ACS APPLIED MATERIALS & INTERFACES

Article

Dominant Factors Governing the Electron Transfer Kinetics and Electrochemical Biosensing Properties of Carbon Nanofiber Arrays

Liangsheng Hu, Xiang Peng, Kaifu Huo, Rongsheng Chen, Jijiang Fu, Yong Li, Lawrence Yoon Suk Lee, Kwok-Yin Wong, and Paul K Chu

ACS Appl. Mater. Interfaces, **Just Accepted Manuscript** • DOI: 10.1021/acsami.6b10100 • Publication Date (Web): 07 Oct 2016

Just Accepted

ACS Publications

ACS Applied Materials & Interfaces is published by the American Chemical Society. 1155 Sixteenth Street N.W., Washington, DC 20036

Dominant Factors Governing the Electron Transfer Kinetics and Electrochemical Biosensing Properties of Carbon Nanofiber Arrays

Liangsheng Hu,[†,§,1] Xiang Peng,[I,1] Kaifu Huo,[*,†] Rongsheng Chen,[‡] Jijiang Fu,[‡] Yong Li,[§] Lawrence Yoon Suk Lee,[§] Kwok-Yin Wong[*,§] and Paul K Chu[*,I]

[†]Wuhan National Laboratory for Optoelectronics (WNLO) and School of Optical and Electronic Information, Huazhong University of Science and Technology, Wuhan 430074, China. E-mail: kfhuo@hust.edu.cn

[‡]State Key Laboratory of Refractories and Metallurgy, Wuhan University of Science and Technology, Wuhan 430081, China

[I]Department of Physics and Materials Science, City University of Hong Kong, Tat Chee Avenue, Kowloon, Hong Kong, China. E-mail: paul.chu@cityu.edu.hk

[§]Department of Applied Biology and Chemical Technology and the State Key Laboratory of Chirosciences, The Hong Kong Polytechnic University, Hung Hom, Hong Kong, China. E-mail: kwok-yin.wong@polyu.edu.hk

[1]These authors contributed equally to this work

KEYWORDS: *carbon electrode, core-shell nanofiber, electron transfer kinetics, electrochemical biosensor, dopamine*

ABSTRACT: Carbon-based electrodes have been widely used in electroanalysis for more than half a century but the factors governing the heterogeneous electron transfer (HET) rate are still unclear. The effects of the exposed edge plane site density, inherent resistance of the carbon electrode, and adjustable resistors on the HET kinetics of several outer- and inner-sphere redox couples including $[Fe(CN)_6]^{3-/4-}$, $Ru(NH_3)_6^{3+/2+}$, $Fe^{3+/2+}$, dopamine, ascorbic acid, and uric acid are investigated using three kinds of carbon electrodes composed of core-shell quasi-aligned nanofiber arrays (QANFAs). The internal resistance is found to be a key factor affecting the ET kinetics and electrochemical biosensing properties. The electrodes exhibit high selectivity and sensitivity in dopamine detection in the presence of ascorbic acid and uric acid. In addition to the promising application to electrochemical biosensing, the core-shell TiC/C QANFAs encompassing a highly electroactive carbon shell and conductive TiC core provide insights into the design and construction of the ideal carbon electrode.

INTRODUCTION

Heterogeneous electron-transfer (HET) processes on solid electrodes are ubiquitous and fundamental phenomena in electrochemistry playing significant roles in molecular electronics, electrochemical energy storage and conversion, as well as sensing.[1-3] Recent reports have underscored the desire for higher HET rates for solid electrodes in these aforementioned applications especially sensing.[1, 4-6] One of the challenges confronting electrochemical sensing is that the voltammetric response is unsatisfactory because of slow HET on the electrode surface and subsequent high overpotentials in electrochemical reactions.[7] Therefore, a high-quality electrode with fast HET between the electrode and analytes is crucial to electrochemical techniques.

Among the various electrode materials, carbon is one of the most widely used due to the good chemical inertness, flexible surface chemistry, large potential window, and low cost.[4-5, 8-10] Many types of carbon-based electrodes have been used in electroanalysis for more than half a century and their electrochemical characteristics have been investigated.[8-11] However, the factors governing the HET rate are still not well understood. The simple potential-dependent HET rates measured from different carbon electrodes are generally believed to be associated with the exposed edge plane site (EPS) or defect site density. It has been shown that the EPS on carbon electrodes leads to fast HET kinetics in many redox couples compared to the basal plane of carbon electrodes. Consequently, most research activities have focused on the construction of carbon electrodes with more exposed EPS and/or further physicochemical treatment to increase the EPS density.[12-15] In practical electrochemical sensing, the redox reactions of the probe molecules occur on the electrode surface followed by electron transfer from the electrode to the external circuit (potentiostat). Therefore, electron transfer may be another important factor

influencing the HET rate and sensing properties in addition to the fraction of EPS, but this issue has mostly been ignored so far. The wide range of peak-to-peak separation (ΔE_p) frequently observed from cyclic voltammetry (CV) from redox systems (typically $Fe(CN)_6^{4-/3-}$) with carbon electrodes may be related to the electron transport process. In fact, sluggish electron transfer rate constants (k_o) have been reported from carbon electrodes despite a large exposed EPS density. [11, 16]

Considering the anisotropic resistivity and electroactivity of graphite, it is hard to prepare a carbon electrode combining high electroactivity with low resistance. Recently, the core-shell quasi-aligned nanofiber arrays (QANFAs) have been demonstrated as one of the significant platforms in electrochemical sensing due to the enhanced properties rendered by the shell and core components as well as resulting synergetic effect.[17-19] We have developed a simple thermochemical method to prepare cylindrical and conical TiO_2/C core-shell QANFAs on Ti with 2.5% and 15.5% EPS coverage.[20] Furthermore, cylindrical TiC/C QANFAs have been produced directly on Ti6Al4V foils by the same method to produce a carbon shell with similar structures as those of TiO_2/C together with a highly conductive TiC core.[17-18] Both the TiO_2/C and TiC/C nanofibers have the same surface states and EPS density, but their cores have different electrical conductivity. However, during the comparative study in measuring $Fe(CN)_6^{3-/4-}$ and dopamine, the better Nernstian behavior is observed from the TiC/C electrode suggesting that the internal resistance may affect the HET kinetics and sensing performance in spite of the lack of clear evidence.

Herein, we illustrate the design of the ideal carbon-based electrode and identify the critical factors influencing the HET kinetics on carbon electrodes including the EPS density and electron conductivity. Three types of core-shell QANFAs are prepared to study how the density of the

exposed EPS and inherent resistance of the electrodes influence the HET kinetics in several outer- and inner-sphere redox systems including $[Fe(CN)_6]^{3-/4-}$, $Ru(NH_3)_6^{3+/2+}$, $Fe^{3+/2+}$, dopamine (DA), ascorbic acid (AA), and uric acid (UA). The two types of electrodes, cylindrical TiO_2/C (**Scheme 1a**) and TiC/C (**Scheme 1b**) QANFAs, have similar surface structures but different cores, whereas the conical TiC/C QANFAs are prepared to compare the effects of the exposed EPS density. To further confirm how the internal resistance influences the HET rates, we conduct control experiments in which the resistance is deliberately introduced to the electrode systems by two methods: (1) QANFAs scraped from the substrate (Ti or Ti6Al4V foil) and then deposited onto a glassy carbon electrode (GCE) to introduce contact resistance and (2) an adjustable resistor connected in series between the working electrode and potentiostat (**Scheme 1c**). This provides a straightforward demonstration of how the internal resistance affects the HET kinetics of the carbon electrode. Our results show that the internal resistance is the key factor governing the HET kinetics and the structure-dependent electrochemical sensing properties described here offer new insights into the design and construction of the ideal carbon electrodes (**Scheme 1b**).

EXPERIMENTAL SECTION

QANFAs Fabrication and Characterization.

Core-shell TiO_2/C and TiC/C QANFAs were fabricated directly on Ti and Ti6Al4V substrates by a thermochemical method described in our previous reports.[17-18, 20-21] In brief, the Ti (10×10×1 mm^3, Advent, 99.5%) and Ti6Al4V (10×10×1 mm^3, Goodfellow) foils were degreased ultrasonically in acetone and ethanol, respectively, followed by polishing in a solution

containing H_2O, HF, and HNO_3 with a volume ratio of 5:1:4 for 5 min to remove the surface native oxide. After rinsing with double-distilled water (DDW) and drying under flowing nitrogen, the Ti and Ti6Al4V foils were put in a ceramic boat-like crucible placed at the center of an alumina tube in a horizontal tube furnace. The reactor system was purged with argon three times to remove residual oxygen and/or moisture before heating to 800 °C (for cylindrical CNFs) or 850 °C (for conical CNFs) at a heating rate of 10 °C min^{-1} in high-purity argon. Acetone was then bled into the chamber together with argon at a flow rate of 150 SCCM. After the thermochemical reaction had proceeded for 90 min, the furnace was gradually cooled to room temperature under argon to produce the TiO_2/C QANFAs on Ti and TiC/C QANFAs on Ti6Al4V. The black products on the Ti and Ti6Al4V foils were characterized by field-emission scanning electron microscopy (FE-SEM, FEI Nova 400 Nano), transmission electron microscopy (TEM), high-resolution TEM (HR-TEM, JEOL, JEM-2100F), Raman scattering spectroscopy (Renishaw 2000), and X-ray photoelectron spectroscopy (XPS, Physical Electronics PHI 5802).

Analytical Measurements and Calculations.

The electrochemical experiments were conducted on a CHI 660c potentiostat (CH Instruments, Shanghai, China). The TiO_2/C and TiC/C QANFAs fabricated on the Ti and Ti6Al4V foils were insulated with epoxy resin to expose an area of 9×9 mm^2 to serve as the working electrode. For comparison, the TiO_2/C or TiC/C nanofibers modified GCE were also prepared. In the typical preparation, a bare GCE was polished with 0.05 μm α-alumina with a polishing cloth, rinsed ultrasonically with DDW, and dried at room temperature before use. The nanofibers produced on Ti or Ti6Al4V foils were scraped off and then dispersed in ethanol (0.5 mg mL^{-1}) ultrasonically for 30 min. About 5 μL of the nanofibers-dispersed suspension were cast on the surface of the GCE and dried in air to serve as the working electrode. Prior to use,

the modified electrode was rinsed with DDW to remove loose nanofibers from the surface and dried in air. The Ag/AgCl electrode and Pt wire were used as the reference electrode and counter electrode, respectively. In the investigation of the internal resistance effects on the HET kinetics for the different electrodes, a controllable resistor was connected in series between the working electrode and potentiostat. Potassium ferricyanide, hexaammineruthenium (III) chloride, Fe_3Cl, DA, AA, and UA and other chemicals were analytical grade unless otherwise stated. DDW was used to prepare the solutions and clean the electrodes. The phosphate buffer solution (PBS, 0.1 M, pH 7.4) was prepared by dissolving NaH_2PO_4 and Na_2HPO_4 in DDW and the pH value was adjusted to 7.4 by adding H_3PO_4 and NaOH.

The electron transfer kinetics was determined by CV. The HET rate constants were determined from ΔE_p using Nicholson's model [22] by assuming $\alpha = 0.5$ and using the following diffusion coefficients: $Fe(CN)_6^{3-/4-}$, $D_O=7.63\times10^{-6}$ cm^2 s^{-1}, $D_R=6.32\times10^{-6}$ cm^2 s^{-1}; $[Ru(NH_3)_6]^{3+/2+,}$ $D_O=6.5\times10^{-6}$ cm^2 s^{-1}; $Fe^{3+/2+}$, $D_O=7.9\times10^{-6}$ cm^2 s^{-1}; DA, $D_O=6.0\times10^{-6}$ cm^2 s^{-1}. In all the cases except $Fe(CN)_6^{3-/4-}$, D_O is equal to D_R in the rate constant calculation. The Nyquist diagrams were obtained by electrochemical impedance spectroscopy (EIS) performed between 100 kHz and 100 mHz on $[Fe(CN)_6]^{3-}$/$[Fe(CN)_6]^{4-}$ (5 mM, 1:1) in 1.0 M KCl.

RESULTS AND DISCUSSION

Characterization of QANFAs.

Figures 1a and 1b depict the representative low-magnification FE-SEM images of the TiO_2/C and TiC/C QANFAs synthesized at 800 ^oC revealing the uniform cylindrical nanofibers

grown *in situ* on Ti or Ti6Al4V foil. Both nanofibers consist of a nanowire core 40 - 50 nm in diameter and shell 15 - 20 nm thick (Insets in **Figures 1a and 1b**). The low-magnification FE-SEM image of the TiC/C QANFAs prepared at 850 ^{o}C shows uniform conical nanofibers (**Figure 1c**) with a core-shell structure (Inset in **Figure 1c**). The core diameter is 30 - 40 nm and shell thickness of the conical TiC/C is 150 nm at the base and <10 nm at the tip. The enlarged FE-SEM images of the TiO_2/C and TiC/C QANFAs (both cylindrical and conical fibers) (**Figure S1**, **Supporting Information, SI**) clearly show that all the produced nanofibers are quasi-aligned.

The Raman scattering spectra acquired from the TiO_2/C and TiC/C QANFAs in **Figure 2a** show the two main D and G bands at 1348 and 1592 cm^{-1}, respectively. The G band shifts from its normal value of 1580 to 1592 cm^{-1} indicating that the carbon shells are made of nanocrystalline graphite or small in-plane sp2 domains.[23] The I_D/I_G ratios of the cylindrical TiC/C and TiO_2/C QANFAs are about 1.66 and 1.69, respectively. The I_D/I_G ratio of the conical TiC/C QANFAs is smaller than that of the cylindrical QANFAs due to the higher crystallinity of the carbon shell of the conical QANFAs as they are prepared at a slightly higher temperature than the cylindrical QANFAs. The XPS spectra acquired from the cylindrical TiC/C and TiO_2/C QANFAs are quite similar showing a strong C 1s peak at 284.5 eV, small O 1s peak at 532.0 eV, and weak Auger band C KLL peak at 1225.0 eV (**Figure 2b**), suggesting the presence of only carbon in the shell with the exception of adsorbed oxygen on the surface. The high-resolution C1s spectra (**Figure 2c**) show that both types of QANFAs have similar surface compositions. The C1s peak can be deconvoluted into three sub-peaks at 284.6, 284.9, and 286.4eV associated with C–C (sp^2), defects, and C-O,[24] respectively. The HR-TEM images show that there are few EPSs (indicated by the arrow) on the surface of both the cylindrical TiO_2/C and TiC/C nanofibers (**Figures 1d and 1e**). According to FE-SEM, Raman scattering, XPS, and HR-TEM,

it can be concluded that the carbon shell on the cylindrical TiO_2/C and TiC/C nanofibers have almost the same macroscopic and microscopic surface texture. The HR-TEM images of the conical TiC/C nanofiber (**Figures 1f and 1g**, respectively) show that decreasing the thickness of the carbon shell from ~60 nm to ~2.5 nm produces the conical shape resulting in a larger EPS density.

Electrochemical Measurements and Analyses.

For comparison, the HET properties of the cylindrical TiO_2/C and TiC/C as well as conical TiC/C QANFAs are determined using the $[Fe(CN)_6]^{3-/4-}$ redox couple which kinetics is sensitive to the microstructure thus providing a probe for the inner-sphere electron transfer pathway.[3] With regard to carbon electrodes, the $[Fe(CN)_6]^{3-/4-}$ redox couple probe is of particular interest because its HET process depends strongly on the EPS density.[10, 25-26] **Figure 3** shows the CV response of the electrodes of the cylindrical TiO_2/C (**Figure 3a**) and TiC/C (**Figure 3b**) as well as conical TiC/C QANFAs (**Figure 3c**) in the 1.0 mM $K_3[Fe(CN)_6]$ solution. All the electrodes show fast HET rates for $[Fe(CN)_6]^{3-/4-}$. The ΔE_p values in **Figures 3a-3c** are plotted against the scanning rate in **Figure 3d**. It can be clearly seen that ΔE_p measured from the TiO_2/C increases steadily from 66 to 119 mV with increasing scanning rates, whereas those of both the cylindrical and conical TiC/C electrodes are constant at 59 mV at scanning rates between 10 and 1000 mV s^{-1} and increase slightly to 64 mV at a scanning rate of 1500 mVs^{-1}. In general, ΔE_p of 59 mV is expected to obey the Nernstian single-electron electrochemical behavior.[3] The results suggest that both the cylindrical and conical TiC/C have the adequate surface structures and electronic properties for rapid HET in this particular redox system. According to Nicholson's model[22], the HET rates of the redox couples exhibit the ideal reversible electrochemical behavior with the estimated k_0 of TiO_2/C being 0.013 cm s^{-1} and that of TiC/C larger than 0.6 cm s^{-1}. As shown in

Figures 1 and 2, the carbon shells of the cylindrical TiO_2/C and TiC/C have similar macro- and micro-structures, and the only difference between the two nanofibers is that the TiO_2/C QANFAs have a semi-conductive TiO_2 core, whereas the TiC/C QANFAs have the conductive TiC. The difference lies in the core conductivity and a larger k_0 is observed from the TiC/C than TiO_2/C. Apparently, the highly conductive core in TiC contributes to the fast HET kinetics as it can offer a good pathway for electron transfer from the surface of the QANFAs to the substrate. On the other hand, the conical TiC/C shows larger charging currents and redox peak currents than the cylindrical TiC/C due to the larger exposed EPS density, whereas both the conical and cylindrical TiC/C show the same ΔE_p of 59 mV at scanning rates between 10 and 1000 mV s^{-1}. Based on these analyses, it can be inferred that the internal resistance of the electrodes has a significant effect on the HET kinetics.

To confirm the hypothesis, two control experiments involving the TiO_2/C and TiC/C nanofibers-modified GCEs, in which contact resistance is introduced to the electrodes, are performed. The CVs obtained from the conical TiC/C nanofiber-modified GCE show larger redox peaks than the other two, indicating that the better performance is probably due to the larger exposed EPS (**Figure S2, SI**). Although all the modified GCEs show smaller ΔE_p than the bare GCE, ΔE_p obtained from the modified GCEs is larger than that of the QANFAs. The failure to take advantage of the conductive core and introduced contact resistance between the nanofibers and GCEs adversely affect the HET process. Therefore, the nanofiber-modified GCEs exhibit larger ΔE_p than the nanofibers prepared *in situ* on the metal foil. Other control experiments are also conducted by introducing an adjustable resistor to the circuit. The CV profiles and corresponding ΔE_p values acquired from the cylindrical TiC/C QANFAs and with different resistors (0-100 Ω) introduced in 1.0 mM aquatic $K_3[Fe(CN)_6]$ are shown in **Figures 4a**

and 4b, which indicate that the introduced resistors alter the CV behavior of the TiC/C electrode. ΔE_p increases monotonically with the resistance bearing the following linear relationship with resistance (R, Ω); ΔE_p (mV) = 59 + 0.523R(Ω) with a correlation coefficient of 0.9932 (**Figure 4b**). It is noted that ΔE_p of TiC/C with 20 Ω resistance is the same (70 mV) as that of the TiO_2/C (**Figure 3a**), both of which are measured at the same scanning rate of 100 mV s^{-1}. We investigate the electrochemical behavior of the 20 Ω-linked cylindrical TiC/C (designated as TiC/C-20Ω) at various scanning rates. Interestingly, the TiC/C-20Ω electrode exhibits almost the same electrochemical behavior (**Figure 4c**) as the TiO_2/C electrode (**Figure 3a**), suggesting that the internal resistance of the TiO_2/C electrode is larger than that of the TiC/C electrode by approximately 20 Ω. We then acquire the CVs of the TiO_2/C and TiC/C electrodes for a broader range of resistances (0-500 Ω, **Figure S3, SI**) and the results are summarized in **Table S1 (SI)**. ΔE_p of both the TiO_2/C and TiC/C electrodes increases linearly with resistance demonstrating that the internal resistance of the carbon electrodes significantly retards the HET kinetics in the $[Fe(CN)_6]^{3-/4-}$ redox couple.

Electrochemical impedance spectroscopy (EIS) is an effective technique to evaluate HET on the electrode.[27] The semicircles observed at high frequencies correspond to the charge transfer limiting process and the charge transfer resistance (R_{ct}) imparts information about the HET processes on the composite interface and electrochemically active surface area. **Figure 4d** shows the EIS of the cylindrical TiO_2/C, TiC/C, and TiC/C-20Ω electrodes. R_{ct} is obtained by fitting the impedance spectra to the Randles equivalent circuit (REC) as illustrated in the inset of **Figure 4d**. After a 20 Ω resistor is introduced, R_{ct} of the TiC/C electrodes increases to 52 Ω from 32 Ω which is almost the same as that of the TiO_2/C electrode (53 Ω) (**Figure 4d**), indicating that the inherent resistance of the TiO_2/C electrode is about 20 Ω larger than that of

the TiC/C electrode. According to the I-V curves (**Figure S4, SI**), the resistance of the TiO_2/C and TiC/C QANFAs is roughly 25.6 Ω and 2.5Ω, respectively.

To obtain more information about the HET processes besides $[Fe(CN)_6]^{3-/4-}$, other redox systems including $Ru(NH_3)_6^{3+/2+}$ and $Fe^{3+/2+}$ are studied using the cylindrical TiC/C, TiC/C-20Ω, TiO_2/C QANFAs electrodes. **Figure 5** shows the CV acquired from 1.0 mM $Ru(NH_3)_6^{3+/2+}$ in 1.0 M KCl and 1.0 mM $Fe^{3+/2+}$ in 1.0 M $HClO_4$ for the TiC/C, TiC/C-20Ω, TiO_2/C QANFAs electrodes, respectively. The voltammetric data and apparent electron transfer rate constants, k_0, are summarized in **Table S2 (SI)**. These redox systems with different electrode kinetics are evaluated because of the well-known sensitivity or insensitivity to the electronic properties, surface microstructure, and surface chemistry of the carbon electrodes. As a simple outer-sphere redox couple, $Ru(NH_3)_6^{3+/2+}$ has an HET rate constant relatively insensitive to the surface microstructure or adsorbed monolayers on the carbon electrodes.[24, 28-29] As shown by the CVs acquired from $Ru(NH_3)_6^{3+/2+}$, the TiO_2/C, TiC/C, and TiC/C-20Ω electrodes have ΔE_p of 67, 53, and 69 mV, respectively (**Figure 5a**). In addition to the small ΔE_p, a k_0 larger than 0.18 cm s^{-1} suggests fast HET kinetics on the TiC/C electrode. Relatively small k_0 values of 0.032 cm s^{-1} and 0.025 cm s^{-1} are calculated from the TiO_2/C and TiC/C-20Ω electrodes, respectively. $Fe^{3+/2+}$, a typical inner-sphere model, has been demonstrated to depend strongly on surface carbon-oxygen functionalities especially carbonyl groups.[30] The three electrodes show slow electron kinetics for the $Fe^{3+/2+}$ redox pairs (**Figure 5b**). ΔE_p in the curve is about 240 mV and consistent with a k_0 (**Table S2, SI**) of 6×10^{-4} cm s^{-1} due to the lack of catalytic carbonyl groups on the carbon shell surface, suggesting that the internal resistance influences the processes of slow HET redox slightly.

To explore possible applications of the TiC/C electrode to biosensing, three essential biomolecules in the body fluids, namely of DA, AA, and UA, are detected. DA is one of the important neurotransmitter compounds and plays a significant role in the central nervous, renal, cardiovascular, and hormonal systems.[31] Abnormal concentrations of DA are closely linked to senile dementia, Parkinson disease, schizophrenia, and HIV infection.[31-33] Unfortunately, DA, AA, and UA generally produce overlapping voltammetric responses on conventional bare metal or carbon electrodes.[34-37] Here, the electrochemical response to DA, AA, and UA on the three electrodes (TiC/C, TiC/C-20Ω, and TiO_2/C) is investigated and **Figure 6a** shows the effects of the internal resistance on DA, AA, and UA voltammetry. The HET rate of DA on the TiC/C electrode is very fast as suggested by an ideal ΔE_p value (29 mV, **Figure 6a**) for a two-electron redox system and k_0 of >0.18 cm s^{-1}. With regard to the TiC/C-20Ω electrode, a ΔE_p of 31 mV (**Figure 6a**) is measured and slightly smaller than that of the TiO_2/C electrode (32 mV, **Figure 6a**). Similar to the $[Fe(CN)_6]^{3-/4-}$ redox mediator, the effects of the internal resistance are evident in the other redox systems with different electrode kinetics. The TiO_2/C electrode with a semiconductor core and TiC/C electrode with the introduced resistance again shows much smaller HET rates. Compared to the TiC/C electrode, the peak potential in response to AA positively shifts 70 mV and 180 mV on the TiC/C-20Ω and TiO_2/C electrodes, respectively, indicating substantially slower HET kinetics [30] not boding well for simultaneous detection of DA, AA, and UA as shown in **Figure 6a** (AA+DA+UA). With regard to UA, the response peak potentials shift slightly while the response current decreases by about 10% on the TiC/C-20Ω and TiO_2/C electrodes in comparison with the TiC/C electrode. The cyclic voltammetric graphs are obtained from the three types of the electrode in PBS containing DA, AA, and UA (**Figure 6a**). The anodic peaks of the ternary mixture of DA, AA, and UA overlap when detected by the

TiC/C-20Ω electrode and TiO_2/C electrodes resulting in one broad peak. In contrast, by using the TiC/C, three notable anodic peaks at -8, 150, and 273 mV corresponding to direct oxidation of AA, DA, and UA, respectively, can be readily discerned. The large separation between the oxidation peak potentials of AA-DA (158 mV), DA-UA (123 mV), and UA-AA (281 mV) allows selective and simultaneous determination of AA, DA, and/or UA in the presence of the other species. Selective determination of DA is monitored by differential pulse voltammetry (DPV) in the presence of AA and UA using various concentrations of DA. **Figure 6b** presents the typical DPV curves obtained from the TiC/C QNFAs electrode in 0.1 M PBS (pH = 7.4) containing 100 μM AA and 10 μM UA and different concentrations of DA between 0 and 170 μM. Three peaks corresponding to oxidation of AA, DA, and UA can be observed. The peak current (y) of DA varies linearly with the DA concentration (x) in the range of 1-120 μM but those of the other two compounds remain unchanged. The linear regression equation is expressed as y (μA) = 0.2766x (μM) - 0.1142 (**Inset in Figure 6b**) with a correlation coefficient of 0.9970. The detection limit of DA is deduced to be 0.055 μM (S/N = 3).

Proposed Electron Transfer Process

The microstructure of the both the cylindrical TiO_2/C and TiC/C is depicted as a "kaleidoscope" (**Schemes 1a and 1b**). The TiO_2/C and TiC/C have a nanotubular shell with a similar amount of defects. Graphitic EPS that inevitably exists on the edge are attributed to discontinuity of the graphite planes. [38] Although the cylindrical TiO_2/C and TiC/C QANFAs have similar carbon shell microstructures, the former consists of a semiconductive rutile TiO_2 core (resistivity of $>3\times10^4$ Ω·cm), [39-40] whereas the latter contains a highly conductive TiC core (resistivity of 6.8×10^{-5} Ω·cm). [41-42] It is well known that the resistivity along the *c*-axis (0.17

Ω·cm [10]) is much larger than that along the *a*-axis (4.5×10^{-5} Ω·cm) [10] in graphite. As shown in **Scheme 1**, when redox reactions take place at the EPS where electrons are exchanged, the electrons are transferred freely in-plane (along *a*-axis direction). In the reactions on the TiC/C electrode surface, the exchanged electrons at the carbon shell can be readily delivered to the TiC core and then rapidly relayed to the underlying Ti6Al4V substrate. In contrast, the exchanged electrons on the TiO_2/C electrode can only move through the inter-plane of the carbon shell (*c*-axis direction) resulting in small HET rates and poor electrochemical sensing properties.

CONCLUSION

Strong evidence about the role of the inherent resistance of the electrode in the HET kinetics in both the inner- and outer-sphere redox reactions is obtained and described. It is important to consider the internal resistance of the electrode in the design and construction of the electrodes in order to obtain the desirable electrochemical performance. Considering the contradictory resistivity and electroactivity of graphite, the core-shell TiC/C architecture composed of a highly electroactive shell and conductive core offers a new route to design the ideal carbon electrode for biosensing and high-power electrochemical energy storage devices.

ASSOCIATED CONTENT

Supporting Information. High-magnification FE-SEM images of TiO_2/C and TiC/C QANFAs (Figure S1); CV curves of 1.0 mM $K_3Fe(CN)_6$ obtained from TiO_2/C and TiC/C nanofiber-modified GCEs (Figure S2); CV curves of 1.0 mM $K_3Fe(CN)_6$ obtained from TiO_2/C and TiC/C

QANFAs connected to 0-500 Ω resistors (Figure S3); I-V characteristics of TiO_2/C and TiC/C QANFAs (Figure S4); obtained from TiC/C and TiO_2/C QANFAs electrodes with various resistance connected in series(Table S1); Variation of ΔE_p and apparent k_0 in the $Ru(NH_3)_6^{3+/2+}$, $Fe^{3+/2+}$and DA redox systems for the cylindrical TiO_2/C, TiC/C and TiC/C-20Ω QANFAs electrodes (Table S2). This material is available free of charge via the Internet at http://pubs.acs.org.

Corresponding Author

E-mail: kfhuo@hust.edu.cn (K.F. Huo); paul.chu@cityu.edu.hk (P.K. Chu); kwok-yin.wong@polyu.edu.hk(K.Y. Wong)

Notes

The authors declare no competing financial interest.

ACKNOWLEDGMENTS

This work was jointly supported by Natural Science Foundation of China (NOs:51572100, 51504171 and 31500783), City University of Hong Kong Applied Research Grant (ARG) No. 9667122, as well as Innovation and Technology Commission of Hong Kong. The TEM experiments were conducted at the Hong Kong Polytechnic University Research Facility in the Materials Characterization and Device Fabrication (UMF)-center for Electron Microscopy. We acknowledge the use of the facilities and engineering support by Dr. Wei Lu.

REFERENCES

(1) Chen, S.; Liu, Y.; Chen, J., Heterogeneous electron transfer at nanoscopic electrodes: importance of electronic structures and electric double layers. *Chem. Soc. Rev.* **2014,** *43* (15), 5372-5386.

(2) Khoshtariya, D. E.; Dolidze, T. D.; Shushanyan, M.; Davis, K. L.; Waldeck, D. H.; van Eldik, R., Fundamental signatures of short-and long-range electron transfer for the blue copper protein azurin at Au/SAM junctions. *Proc. Natl. Acad. Sci. U.S.A.* **2010,** *107* (7), 2757-2762.

(3) Bard, A. J.; Faulkner, L. R., *Electrochemical methods: fundamentals and applications*. Wiley New York: **2010**, pp. 87-132.

(4) Chen, R.; Nioradze, N.; Santhosh, P.; Li, Z.; Surwade, S. P.; Shenoy, G. J.; Parobek, D. G.; Kim, M. A.; Liu, H.; Amemiya, S., Ultrafast Electron Transfer Kinetics of Graphene Grown by Chemical Vapor Deposition. *Angew. Chem. Int. Ed.* **2015,** *54*, 15134-15137.

(5) Zhou, M.; Guo, S., Electrocatalytic Interface Based on Novel Carbon Nanomaterials for Advanced Electrochemical Sensors. *ChemCatChem* **2015,** *7* (18), 2744-2764.

(6) Zhang, Y.; Chu, M.; Yang, L.; Tan, Y.; Deng, W.; Ma, M.; Su, X.; Xie, Q., Three-Dimensional Graphene Networks as a New Substrate for Immobilization of Laccase and Dopamine and Its Application in Glucose/O_2 Biofuel Cell. *ACS Appl. Mater. Interfaces* **2014,** *6* (15), 12808-12814.

(7) Zoski, C.; Miao, W., Handbook of electrochemistry. *Las Cruces-New Mexico, Ed Thomson*. 2007, pp. 3-18.

(8) Zhang, W.; Zhu, S.; Luque, R.; Han, S.; Hu, L.; Xu, G., Recent development of carbon electrode materials and their bioanalytical and environmental applications. *Chem. Soc. Rev.* **2016,** *45*, 715-752.

(9) Ratinac, K. R.; Yang, W.; Gooding, J. J.; Thordarson, P.; Braet, F., Graphene and related materials in electrochemical sensing. *Electroanalysis* **2011,** *23* (4), 803-826.

(10) McCreery, R. L., Advanced carbon electrode materials for molecular electrochemistry. *Chem. Rev* **2008,** *108* (7), 2646-2687.

(11) Ambrosi, A.; Chua, C. K.; Bonanni, A.; Pumera, M., Electrochemistry of graphene and related materials. *Chem. Rev.* **2014,** *114* (14), 7150-7188.

(12) Zhong, J.-H.; Zhang, J.; Jin, X.; Liu, J.-Y.; Li, Q.; Li, M.-H.; Cai, W.; Wu, D.-Y.; Zhan, D.; Ren, B., Quantitative correlation between defect density and heterogeneous electron transfer rate of single layer graphene. *J. Am. Chem. Soc.* **2014,** *136* (47), 16609-16617.

(13) Zhang, B.; Fan, L.; Zhong, H.; Liu, Y.; Chen, S., Graphene nanoelectrodes: fabrication and size-dependent electrochemistry. *J. Am. Chem. Soc.* **2013,** *135* (27), 10073-10080.

(14) Gong, K.; Chakrabarti, S.; Dai, L., Electrochemistry at carbon nanotube electrodes: Is the nanotube tip more active than the sidewall? *Angew. Chem. Int. Ed.* **2008,** *47* (29), 5446-5450.

(15) Brownson, D. A.; Kampouris, D. K.; Banks, C. E., Graphene electrochemistry: fundamental concepts through to prominent applications. *Chem. Soc. Rev.* **2012,** *41* (21), 6944-6976.

(16) Wang, J.; Yang, S.; Guo, D.; Yu, P.; Li, D.; Ye, J.; Mao, L., Comparative studies on electrochemical activity of graphene nanosheets and carbon nanotubes. *Electrochem. Commun.* **2009,** *11* (10), 1892-1895.

(17) Hu, L.S.; Huo, K.; Chen, R.; Zhang, X.; Fu, J.; Chu, P. K., Core–shell TiC/C quasi-aligned nanofiber arrays on biomedical Ti6Al4V for sensitive electrochemical biosensing. *Chem. Commun.* **2010,** *46* (36), 6828-6830.

(18) Liu, J. T.; Hu, L. S.; Liu, Y. L.; Chen, R. S.; Cheng, Z.; Chen, S. J.; Amatore, C.; Huang, W. H.; Huo, K. F., Real Time Monitoring of Auxin Vesicular Exocytotic Efflux from Single Plant Protoplasts by Amperometry at Microelectrodes Decorated with Nanowires. *Angew. Chem. Int. Ed.* **2014,** *53* (10), 2643-2647.

(19) Li, L.M.; Wang, X.Y.; Hu, L.S.; Chen, R.S.; Huang, Y.; Chen, S.J.; Huang, W.H.; Huo, K.F.; Chu, P. K., Vascular lumen simulation and highly-sensitive nitric oxide detection using three-dimensional gelatin chip coupled to TiC/C nanowire arrays microelectrode. *Lab on a Chip* **2012,** *12* (21), 4249-4256.

(20) Chen, R.S.; Hu, L.S.; Huo, K.F.; Fu, J.J.; Ni, H.W.; Tang, Y.; Chu, P. K., Controllable growth of conical and cylindrical TiO2–carbon core–shell nanofiber arrays and morphologically dependent electrochemical properties. *Chem. Eur. J.* **2011,** *17* (51), 14552-14558.

(21) Zhang, X.M.; Huo, K.F.; Wang, H.R.; Gao, B.; Fu, J.J.; Hung, T.F.; Chu, P. K., Controlled fabrication of core–shell TiO_2/C and TiC/C nanofibers on Ti foils and their field-emission properties. *ACS Appl. Mater. Interfaces* **2012,** *4* (2), 1037-1042.

(22) Nicholson, R. S., Theory and Application of Cyclic Voltammetry for Measurement of Electrode Reaction Kinetics. *Anal. Chem.* **1965,** *37* (11), 1351-1355.

(23) Ferrari, A. C.; Robertson, J., Interpretation of Raman spectra of disordered and amorphous carbon. *Phys. Rev. B* **2000,** *61* (20), 14095.

(24) Shang, N. G.; Papakonstantinou, P.; McMullan, M.; Chu, M.; Stamboulis, A.; Potenza, A.; Dhesi, S. S.; Marchetto, H., Catalyst‐free efficient growth, orientation and biosensing properties of multilayer graphene nanoflake films with sharp edge planes. *Adv. Funct. Mater.* **2008,** *18* (21), 3506-3514.

(25) Bowling, R. J.; Packard, R. T.; McCreery, R. L., Activation of highly ordered pyrolytic graphite for heterogeneous electron transfer: relationship between electrochemical performance and carbon microstructure. *J. Am. Chem. Soc.* **1989,** *111* (4), 1217-1223.

(26) Rice, R. J.; Pontikos, N. M.; McCreery, R. L., Quantitative correlations of heterogeneous electron-transfer kinetics with surface properties of glassy carbon electrodes. *J. Am. Chem. Soc.* **1990,** *112* (12), 4617-4622.

(27) Orazem, M. E.; Tribollet, B., *Electrochemical impedance spectroscopy*. John Wiley & Sons: **2011**; Vol. 48, pp.20.

(28) Tang, L.; Wang, Y.; Li, Y.; Feng, H.; Lu, J.; Li, J., Preparation, structure, and electrochemical properties of reduced graphene sheet films. *Adv. Funct. Mater.* **2009,** *19* (17), 2782-2789.

(29) Pacios, M.; Del Valle, M.; Bartroli, J.; Esplandiu, M., Electrochemical behavior of rigid carbon nanotube composite electrodes. *J. Electroanal. Chem.* **2008,** *619*, 117-124.

(30) Ranganathan, S.; Kuo, T.-C.; McCreery, R. L., Facile preparation of active glassy carbon electrodes with activated carbon and organic solvents. *Anal. Chem.* **1999,** *71* (16), 3574-3580.

(31) Dong, X.; Wang, X.; Wang, L.; Song, H.; Zhang, H.; Huang, W.; Chen, P., 3D graphene foam as a monolithic and macroporous carbon electrode for electrochemical sensing. *ACS Appl. Mater. Interfaces* **2012,** *4* (6), 3129-3133.

(32) Huang, Y.; Miao, Y.-E.; Ji, S.; Tjiu, W. W.; Liu, T., Electrospun carbon nanofibers decorated with Ag–Pt bimetallic nanoparticles for selective detection of dopamine. *ACS Appl. Mater. Interfaces* **2014,** *6* (15), 12449-12456.

(33) Mercante, L. A.; Pavinatto, A.; Iwaki, L. E.; Scagion, V. P.; Zucolotto, V.; Oliveira Jr, O. N.; Mattoso, L. H.; Correa, D. S., Electrospun polyamide 6/poly (allylamine hydrochloride) nanofibers functionalized with carbon nanotubes for electrochemical detection of dopamine. *ACS Appl. Mater. Interfaces* **2015,** *7* (8), 4784-4790.

(34) Jiang, L.; Nelson, G. W.; Abda, J.; Foord, J. S., Novel Modifications to Carbon-Based Electrodes to Improve the Electrochemical Detection of Dopamine. *ACS Appl. Mater. Interfaces* **2016**, DOI: 10.1021/acsami.6b03879.

(35) Wightman, R. M.; May, L. J.; Michael, A. C., Detection of dopamine dynamics in the brain. *Anal. Chem.* **1988,** *60* (13), 769A-779A.

(36) Mo, J. W.; Ogorevc, B., Simultaneous measurement at dopamine and ascorbate at their physiological levels using voltammetric microprobe based on overoxidized poly(1,2-phenylenediamine)-coated carbon fiber. *Anal. Chem.* **2001,** *73* (6), 1196-1202.

(37) Martin, C., The Parkinson's puzzle—new developments in our understanding of Parkinson's disease have generated a number of promising new treatments for this disabling condition. *Chem. Br.* **1998,** *34 (9),* 40-42.

(38) Syed, L. U.; Liu, J.; Prior, A. M.; Hua, D. H.; Li, J., Enhanced electron transfer rates by AC voltammetry for ferrocenes attached to the end of embedded carbon nanofiber nanoelectrode arrays. *Electroanalysis* **2011,** *23* (7), 1709-1717.

(39) Cronemeyer, D. C., Electrical and optical properties of rutile single crystals. *Phys. Rev.* **1952,** *87* (5), 876.

(40) Breckenridge, R. G.; Hosler, W. R., Electrical properties of titanium dioxide semiconductors. *Phys. Rev.* **1953,** *91* (4), 793.

(41) Zou, G.; Wang, H.; Mara, N.; Luo, H.; Li, N.; Di, Z.; Bauer, E.; Wang, Y.; McCleskey, T.; Burrell, A., Chemical solution deposition of epitaxial carbide films. *J. Am. Chem. Soc.* **2010,** *132* (8), 2516-2517.

(42) Huang, H.; Feng, T.; Gan, Y.; Fang, M.; Xia, Y.; Liang, C.; Tao, X.; Zhang, W., TiC/NiO core/shell nanoarchitecture with battery-capacitive synchronous lithium storage for high-performance lithium-ion battery. *ACS Appl. Mater. Interfaces* **2015,** *7* (22), 11842-11848.

Figure Captions

Scheme 1. Proposed microstructures of cylindrical (a) TiO_2/C and (b) TiC/C QANFAs electrodes and the electron transfer process during the electrochemical reaction. (c) Schematics of the electrochemical test setup with an adjustable resistor introduced to the circuit. WE: working electrode, CE: counter electrode, RE: reference electrode, and R: adjustable resistor. CV profiles (upside) of $Fe(CN)_6^{4-/3-}$ obtained from corresponding electrodes.

Figure 1. Representative low-magnification FE-SEM images of the cylindrical (a) TiO_2/C and (b) TiC/C, and (c) conical TiC/C QANFAs. The insets are TEM images of the corresponding nanofibers. Representative HR-TEM images of the cylindrical (d) TiO_2/C and (e) TiC/C nanofiber as well as (f) middle and the (g) tip of the conical TiC/C nanofiber.

Figure 2. (a) Raman spectra of cylindrical TiO_2/C, TiC/C, and conical TiC/C QANFAs acquired from as-synthesized products on Ti or Ti6Al4V foil. XPS (b) survey scans of the cylindrical TiO_2/C and TiC/C QANFAs prepared on Ti and Ti6Al4V and (c) high-resolution C 1s spectra.

Figure 3. CV profiles obtained from 1.0 mM $K_3Fe(CN)_6$ in 1.0 M KCl for (a) cylindrical TiO_2/C, (b) cylindrical TiC/C, and (c) conical TiC/C QANFAs at different scanning rates. (d) Plots of ΔE_p versus scanning rates.

Figure 4. (a) CV profiles of 1.0 mM $K_3Fe(CN)_6$ in 1.0 M KCl at a scan rate of 100 mV/s from the cylindrical TiC/C connected with a 0-100Ω resistor and (b) plots of ΔE_p versus introduced resistance. (c) CV profiles of 1.0 mM $K_3Fe(CN)_6$ in 1.0 M KCl at scannint rates from 10 to 1500 mV s^{-1} from the cylindrical TiC/C-20Ω. (d) Nyquist diagram of EIS recorded at TiO_2/C, TiC/C and TiC/C-20Ω with the inset in (d) showing the REC model.

Figure 5. Cyclic voltammograms of (a) 1.0 mM $Ru(NH_3)_6^{3+/2+}$ in 1 M KCl and (b) 1.0 mM $Fe^{2+/3+}$ in 0.1 M $HClO_4$ obtained from the TiC/C (black), TiC/C-20Ω (red), and TiO_2/C (blue) QANFAs electrodes. Scanning rate: 100 mV·s^{-1}.

Figure 6. (a) Cyclic voltammograms of 1.0 mM AA, 0.1 mM DA and 0.1 mM UA and their mixture in PBS (0.1M, pH 7.4) at a scan rate of 100 mV s^{-1} obtained from the TiC/C (black), TiC/C-20Ω (red), and TiO_2/C (blue) QANFAs electrodes. (b) DPVs at TiC/C QANFAs electrode in PBS (0.1 M, pH 7.4) containing 100 μM AA, 10 μM UA and different concentrations of DA from 0 to 170 μM. Pulse width = 0.2 s, amplitude = 0.05 V, sample period = 0.0167s and, pulse period = 0.5 s. Inset in (b) is the corresponding calibration curve of respond currents versus the concentration of DA. The error bars represent the respond currents of three independent experiments.

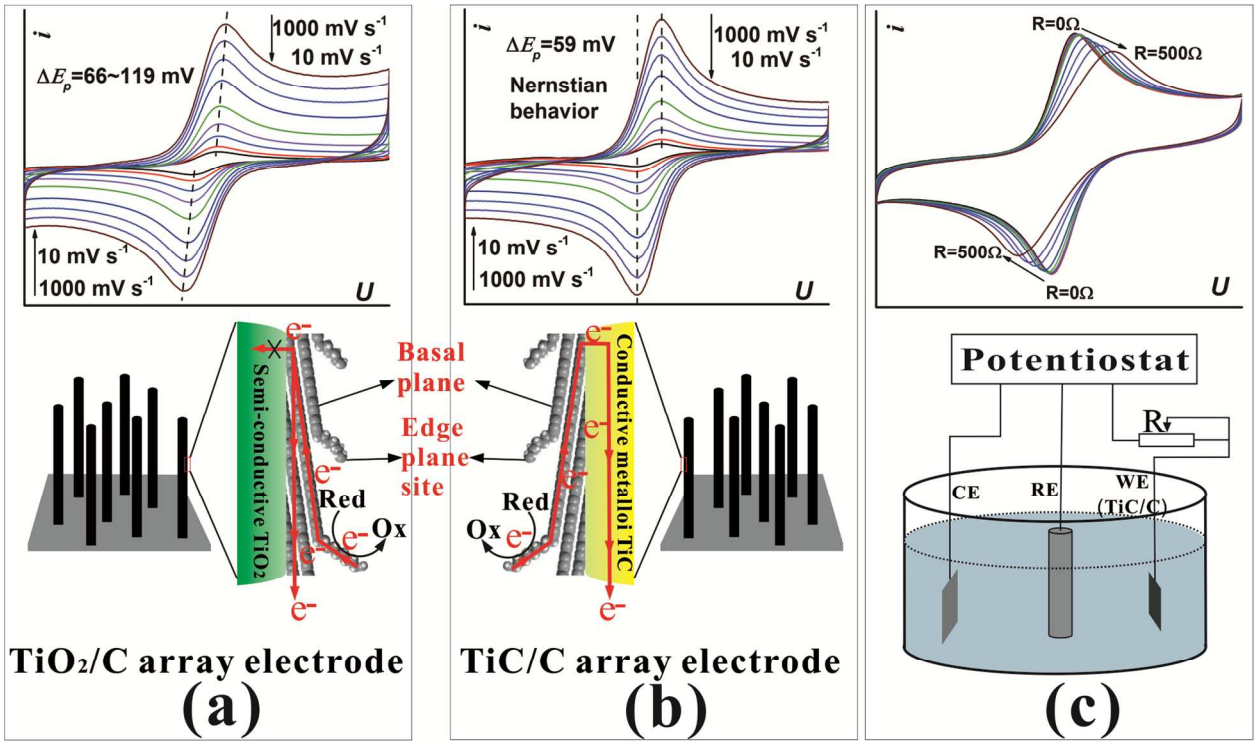
i
ΔEp=66~119 mV
1000 mV s-1
10 mV s-1
10 mV s-1
1000 mV s-1
U
Semi-conductive TiO2
Basal plane
Edge plane site
Red
Ox
TiO2/C array electrode
(a)
ΔEp=59 mV
Nernstian behavior
Conductive metalloi TiC
TiC/C array electrode
(b)
R=0Ω
R=500Ω
Potentiostat
R
CE
RE
WE (TiC/C)
(c)

Scheme 1.

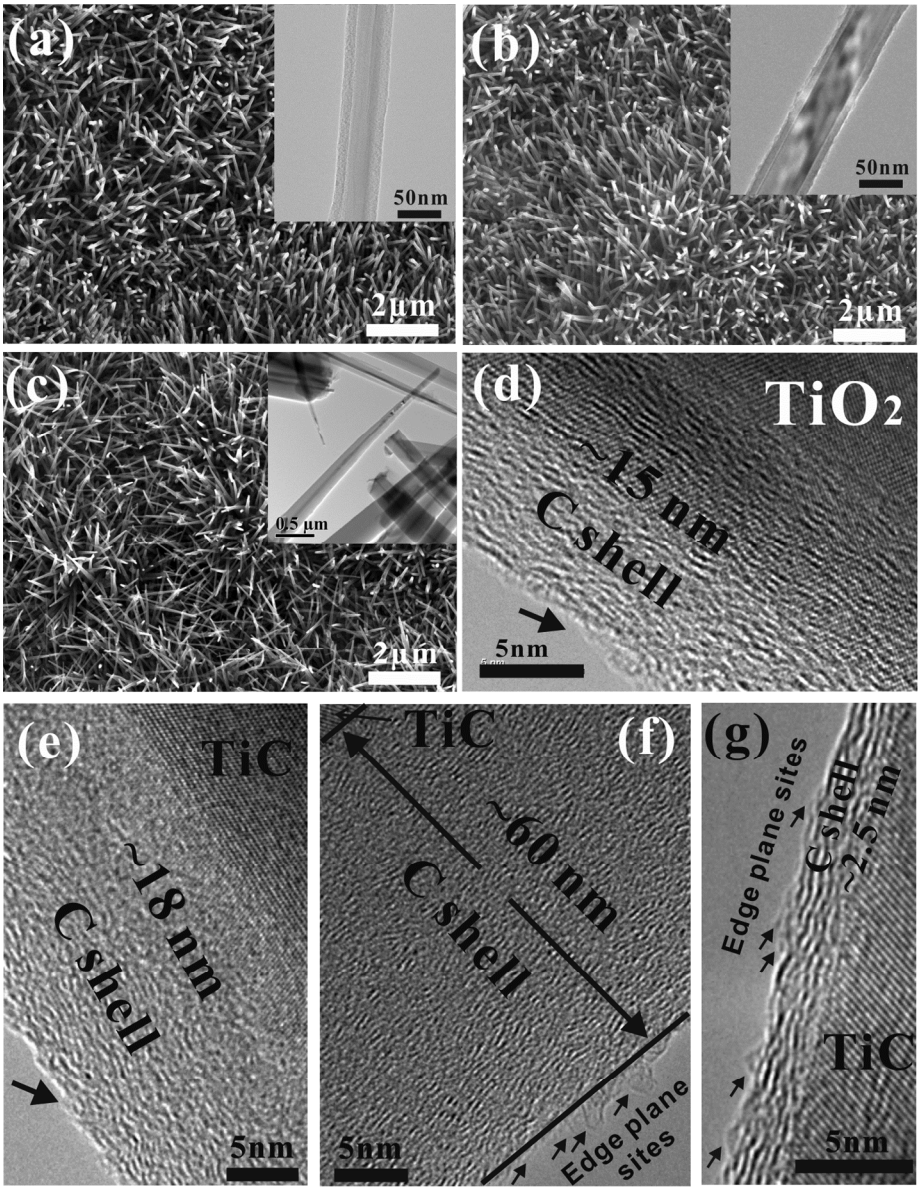
(a)
50nm
2μm
(b)
50nm
2μm
(c)
0.5 μm
2μm
(d)
TiO2
~15 nm
C shell
5nm
(e)
TiC
~18 nm
C shell
5nm
TiC
(f)
~60 nm
C shell
5nm
Edge plane sites
(g)
Edge plane sites
C shell
~2.5 nm
TiC
5nm

Figure 1.

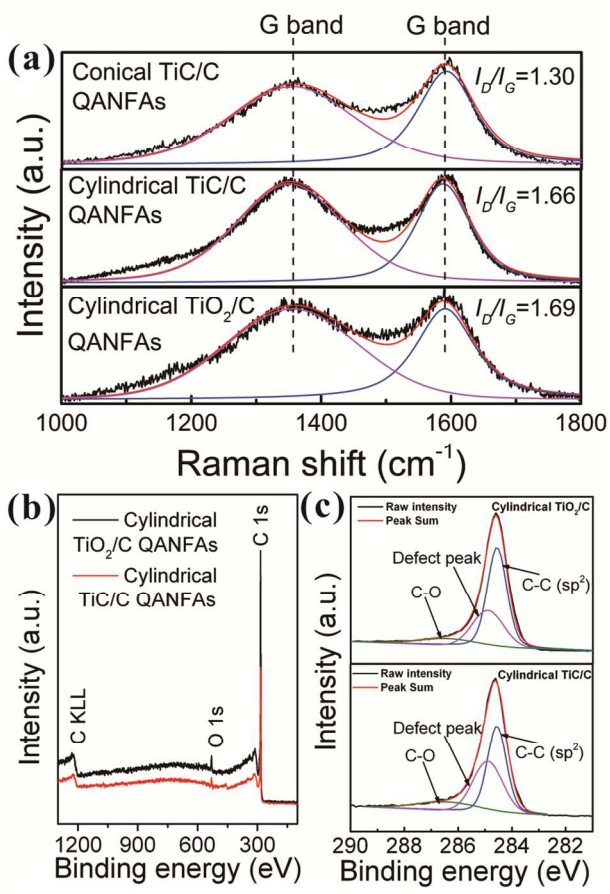
(a)
G band
G band
Conical TiC/C QANFAs
I_D/I_G=1.30
Cylindrical TiC/C QANFAs
I_D/I_G=1.66
Cylindrical TiO_2/C QANFAs
I_D/I_G=1.69
Intensity (a.u.)
1000 1200 1400 1600 1800
Raman shift (cm^{-1})
(b)
Cylindrical TiO_2/C QANFAs
Cylindrical TiC/C QANFAs
C 1s
C KLL
O 1s
Intensity (a.u.)
1200 900 600 300
Binding energy (eV)
(c)
Raw intensity
Peak Sum
Cylindrical TiO_2/C
Defect peak
C-O
C-C (sp^2)
Cylindrical TiC/C
Intensity (a.u.)
290 288 286 284 282
Binding energy (eV)

Figure 2.

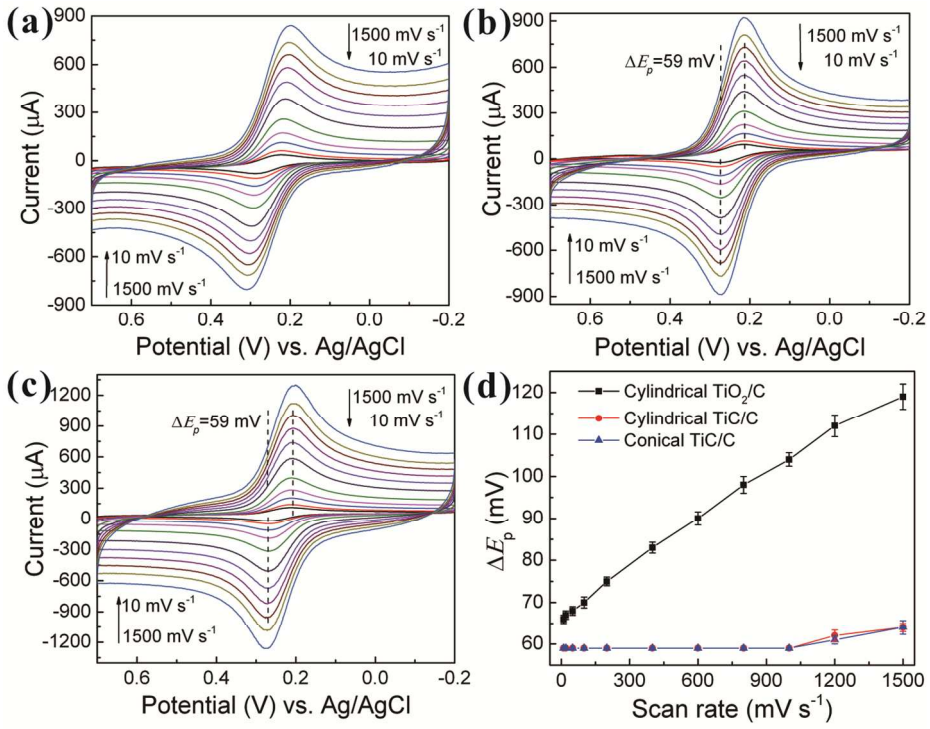
(a)
1500 mV s-1
10 mV s-1
10 mV s-1
1500 mV s-1
Current (μA)
Potential (V) vs. Ag/AgCl
(b)
ΔEp=59 mV
1500 mV s-1
10 mV s-1
10 mV s-1
1500 mV s-1
Current (μA)
Potential (V) vs. Ag/AgCl
(c)
ΔEp=59 mV
1500 mV s-1
10 mV s-1
10 mV s-1
1500 mV s-1
Current (μA)
Potential (V) vs. Ag/AgCl
(d)
Cylindrical TiO2/C
Cylindrical TiC/C
Conical TiC/C
ΔEp (mV)
Scan rate (mV s-1)

Figure 3.

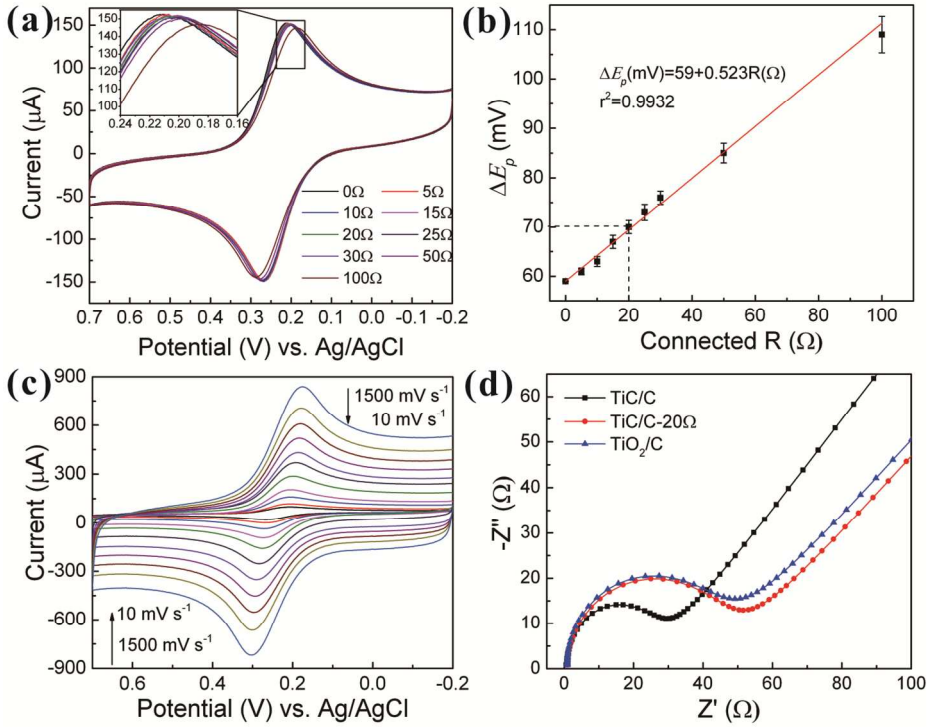
(a)
Current (μA)
Potential (V) vs. Ag/AgCl
0Ω
5Ω
10Ω
15Ω
20Ω
25Ω
30Ω
50Ω
100Ω
(b)
ΔE_p (mV)
ΔE_p(mV)=59+0.523R(Ω)
r²=0.9932
Connected R (Ω)
(c)
Current (μA)
1500 mV s⁻¹
10 mV s⁻¹
10 mV s⁻¹
1500 mV s⁻¹
Potential (V) vs. Ag/AgCl
(d)
-Z'' (Ω)
TiC/C
TiC/C-20Ω
TiO2/C
Z' (Ω)

Figure 4.

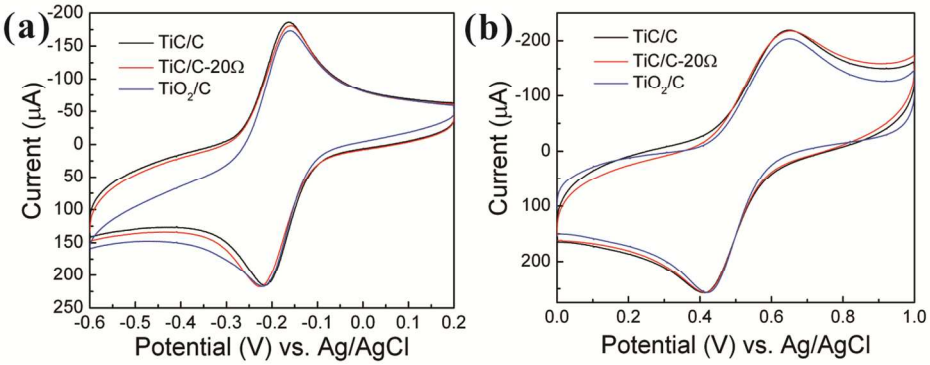

Figure 5.

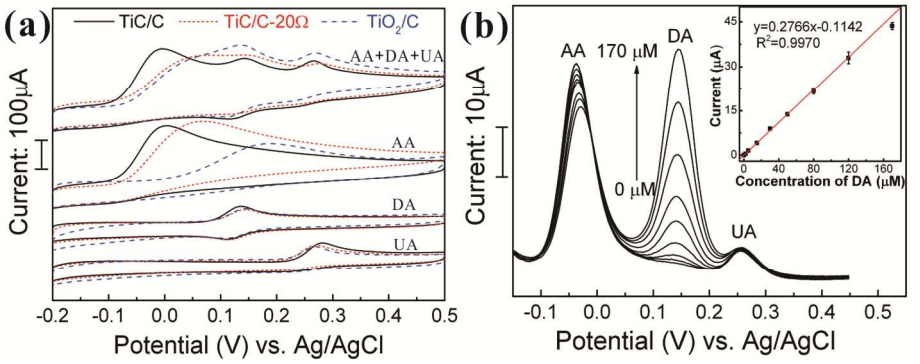

Figure 6.

Table of Contents Graphic